Available online at https://jonass.meybod.iau.ir/

Journal of Nature and Spatial Sciences

Journal homepage: https://jonass.meybod.iau.ir/

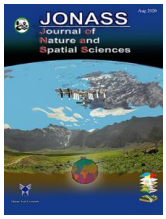

Research Article

Subsidence risk zoning in Varamin County based on effective criteria using TOPSIS and VIKOR techniques

Ali Taheri[a,*], Moslem Dehnavi Eelagh[b]

[a] *Master's student of Geospatial Information Systems, School of Surveying Engineering and Geospatial Information, College of Engineering, University of Tehran, Tehran, Iran*

[b] *Ph.D. student of Geospatial Information Systems, School of Surveying Engineering and Geospatial Information, College of Engineering, University of Tehran, Tehran, Iran*

ARTICLE INFO

Article history:
Receive Date: 10 June 2023
Revise Date: 10 October 2023
Accept Date: 14 October 2023

Keywords:
Subsidence
TOPSIS
VIKOR
DInSAR
Sentinel-1

ABSTRACT

Background and objective: Subsidence is a crisis that modern societies are currently facing. It has the potential to inflict irreparable damage to the lives and properties of residents, as well as disrupt urban infrastructure, including water, oil, and gas transmission lines. While horizontal displacement is also possible, its extent is typically minor. Subsidence results in the formation of cracks and fissures in the ground, alterations in underground water quality, changes to the Earth's surface topography, and other related issues.

Materials and methods: In this study, using the multi-criteria decision-making approach, the seven criteria have been taken into account to produce subsidence risk map. At first, expert opinion on this issue have been used to investigate the effect of different criteria on subsidence. Then the weight of each criterion was obtained using the geometric mean method. Then to combine the layers, VIKOR and TOPSIS fusion techniques were used. To evaluate the implemented method, Sentinel 1 radar images were used to prepare a subsidence map, and a comparison between the two maps has been made.

Results and conclusion: The analysis indicated that land use, underground water, and rainfall had the most significant influence on subsidence, with weights of 0.4292, 0.2699, and 0.1473, respectively. In contrast, slope and elevation had the least impact, with weights of 0.0220 and 0.0375, respectively. A subsidence map was successfully produced using Sentinel-1 images and Differential Interferometric Synthetic-Aperture Radar (DInSAR) techniques, and this map was compared to those obtained through VIKOR and TOPSIS methods, demonstrating a favorable level of compatibility.

1. Introduction

Subsidence is a critical issue that contemporary societies are grappling with, capable of inflicting irrevocable harm to people's lives, property, and urban infrastructure, including water, oil, and gas

* *Corresponding author.* Tel.: +98-902-076-6948
E-mail address: alitaheri1996@ut.ac.ir , ORCID: 0000-0002-4071-2104

Peer review under responsibility of Meybod Branch, Islamic Azad University

2783-1604/© 2023 Published by Meybod Branch, Islamic Azad University. This is an open access article under the CC BY license (https://creativecommons.org/licenses/by/4.0/)

DOI: https://doi.org/10.30495/jonass.2023.1988434.1074

transmission lines. Subsidence represents the gradual or, in some instances, sudden downward displacement of the Earth's surface. Although horizontal displacement can occur, its extent is typically minimal (Water, 2000). Research findings indicate that land subsidence poses a threat to more than 14% of the Earth's surface with a likelihood of over 50%, and approximately 19% of the global population is at risk of subsidence (Herrera-García et al., 2021). Natural and human factors contribute to subsidence, with soil compaction due to declining groundwater levels, particularly significant (Pacheco et al., 2006). Additionally, karst processes, wherein soluble rock layers dissolve in groundwater, can be influential in the development of subsidence. One of the leading causes of land subsidence in arid regions is the extensive extraction of groundwater. Excessive extraction and drainage of groundwater can result in the desiccation of organic soils and the depletion of underground aquifers (Galloway et al., 1999). Subsidence also wreaks havoc on irrigation canals, causing pipeline failures, disrupting power transmission lines, and damaging structures, while also exacerbating landslides and floods.

Furthermore, subsidence leads to the formation of ground cracks and fissures, alterations in the patterns of underground and surface water flow, shifts in underground water quality, modifications to the Earth's surface topography, local flooding, and other consequences. In Iran, this issue holds significant importance, as subsidence has inflicted substantial damage to vital facilities and infrastructures in various regions, especially arid and desert areas of the country, such as Isfahan, Semnan, Yazd, and the southern parts of Tehran province, among others (Dehghani et al., 2013). Hence, this study investigates the potential for subsidence in the cities of Varamin, Qarchak, and Pishva. Subsequently, it reviews the body of research conducted in this field.

Various methods have been employed to assess subsidence risk zoning. These methods encompass Interferometric Synthetic Aperture Radar (InSAR) (Tomás et al., 2014; Calderhead et al., 2011; Anderssohn et al., 2008; Motagh et al., 2007), multi-criteria decision-making (MCDM) (Arabameri et al., 2021; Nadiri et al., 2021; Hwang et al., 1981), probability-based techniques (Galve et al., 2009), artificial intelligence-based approaches (Abdollahi et al., 2019; Lee et al., 2012; Mohammady et al., 2019; Mohammady et al., 2021; Tien Bui et al., 2018; Toomanian et al.), and regression modeling methods such as geographic weighted regression (GWR) and ordinary least squares regression (OLSR) (Kidanu et al., 2018). Below, we highlight several recent studies.

In a study by Najafi et al. (2020), changes in underground water were assessed using Google Earth Engine (GEE), and potential subsidence was mapped using two probabilistic models—the intuitive belief function and Bayesian probability theory. The results indicated that excessive groundwater extraction, elevation, and distance from rivers were the most influential factors, with Bayesian probability theory providing higher accuracy.

Mohammady et al. (2021) modeled land subsidence and created a potential subsidence map using various machine learning methods, including multivariate adaptive regression spline (MARS), mixture discriminant analysis (MDA), and boosted regression tree (BRT). The AUC metric was used to evaluate map accuracy, with MARS, MDA, and BRT found to be the most accurate to the least accurate.

Nadiri et al. (2021) combined MCDM and artificial intelligence approaches to generate a subsidence risk map. They employed a fuzzy catastrophe scheme (FCS) as an MCDM approach and a support vector machine (SVM) as an artificial intelligence approach. The results suggested that subsidence risk in the studied area was primarily due to inherent vulnerability, with human activities playing a lesser role.

Abdollahi et al. (2019) assessed land subsidence potential using the SVM model with different kernel functions. Various factors influencing land subsidence, such as slope percentage, aspect, elevation, and others, were considered. The ROC curve revealed that SVM-produced subsidence potential maps were highly accurate, identifying significant influencing factors.

Mohammady et al. (2019) employed the random forest (RF) machine learning technique to evaluate land subsidence sensitivity. Factors including distance from fault, elevation, slope angle, land use, and water level were found to have the greatest impact on subsidence. The RF algorithm demonstrated acceptable accuracy, with an AUC value of 0.77.

Ebrahimy et al. (2020) produced and compared land subsidence susceptibility maps using BRT, RF, and classification and regression tree (CART), considering numerous influential variables. BRT outperformed RF and CART in terms of prediction accuracy, based on the area under the ROC curve and statistical indices.

Mehrnoor et al. (2023) conducted risk zoning for subsidence based on nineteen criteria, incorporating factors like groundwater loss, groundwater withdrawal, aquifer thickness, land cover, and more. The best-worst model (BWM) and the weight overlap index were used to merge layers, highlighting the significance of factors like groundwater withdrawal and geological formation in subsidence risk.

Abedini et al. (2023) assessed subsidence risk zoning based on various factors, including slope, land use, lithology, and distance from faults and waterways. ANP and MABAC methods were employed for weighting and analysis, revealing water level drop, distance from the river, and lithology as the most influential factors.

In this study, a novel approach was used to generate a potential subsidence map for risk analysis. The criteria considered included groundwater level reduction, rain, slope, elevation, land use, soil type, and TWI. Expert opinions from professionals in the field were utilized to assess the influence of these criteria, and weights were calculated using the geometric mean method. MCDM-based methods, specifically VIKOR (VIseKriterijumska Optimizacija I Kompromisno Resenje) and TOPSIS (Technique for Order Preference by Similarity to Ideal Solution), were applied to combine the layers and produce the final map. Subsequently, these maps were compared and evaluated against maps generated using radar interferometry techniques.

2. Material and Methods

2.1. Case study

Varamin, Pishva, and Qarchak are among the cities of Tehran province, located in the southeast of Tehran city. Varamin City is bounded by Peshwa and Pakdasht cities from the northeast, Qarchak City from the northwest, Ray City from the west, Qom Province from the south, and Semnan Province from the southeast and east. The target area in this study was the cities of Varamin, Pishva, and Qarchak, and the geographical location of these three cities is shown in Figure 1. The studied area has an average elevation of 918 meters above sea level, is close to Iran’s central desert, and has a dry and semi-desert climate.

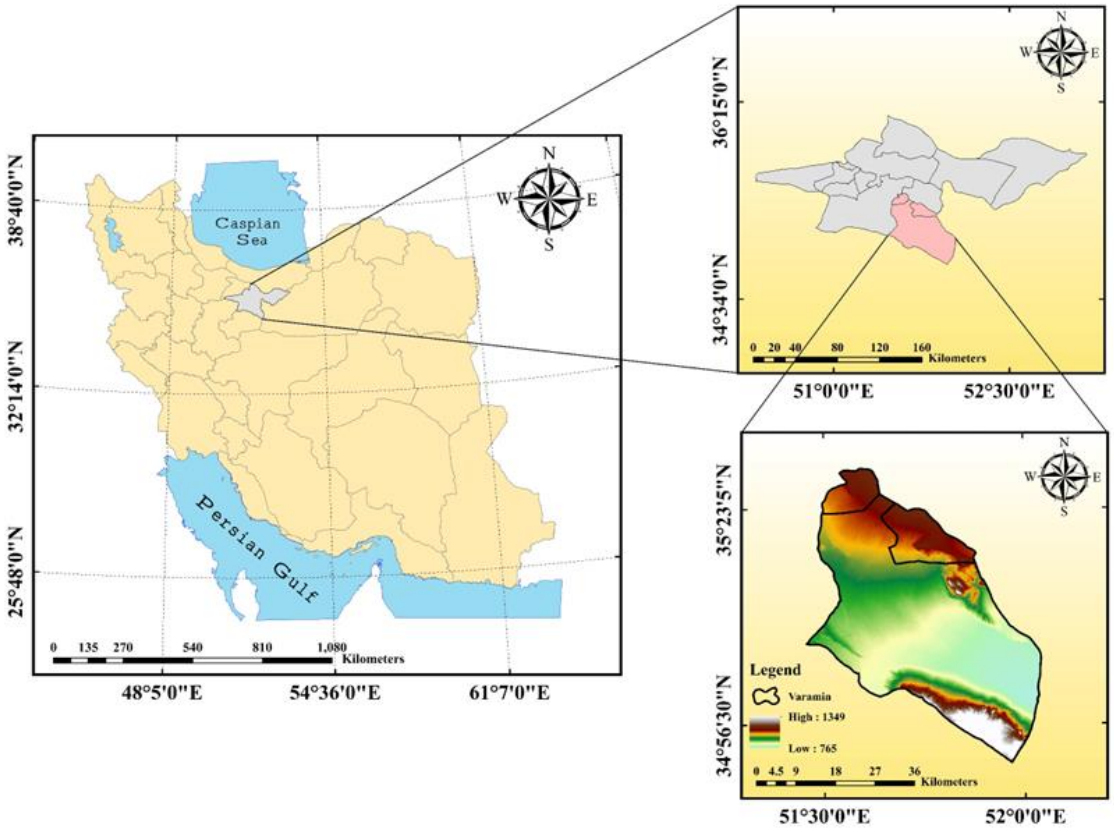

Figure. 1 - Geographical location of the study area

2.2. Datasets

The studied area has 50 piezometric wells, and the information related to these data sets has been collected from Iran water resource management company and prepared point by point from 2014 to 2018. Also, the digital elevation model (DEM) of the area with a resolution of 10 meters has been used that was prepared using Interferometric synthetic-aperture radar (InSAR) technique and information such as slope and TWI has been obtained from the DEM of the area. Also, among the layers that influence the subsidence phenomenon, we can mention the type of soil and land use considered in this study. To produce the land use status of the studied area, Landsat-8 data of the area in 2018 has been used. To generate the rain layer, firstly, raster format data that are produced globally were used. Considering that the raster data had a low resolution, in order to increase the resolution, raster to point analysis was first used to create the center of the pixels as points with specific rain. Then, using the IDW interpolation method, a rain map was produced with a resolution of 10 meters. Figure 2 shows the spatial map of the different layers used in this study. All layers are produced with a resolution of 10 meters.

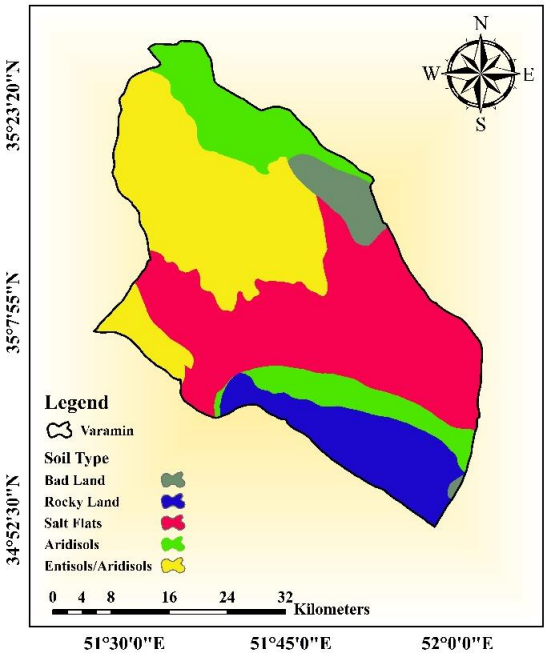
N
W
E
S
35°23'20"N
35°7'55"N
34°52'30"N
Legend
Varamin
Soil Type
Bad Land
Rocky Land
Salt Flats
Aridisols
Entisols/Aridisols
0 4 8 16 24 32
Kilometers
51°30'0"E
51°45'0"E
52°0'0"E

(a)

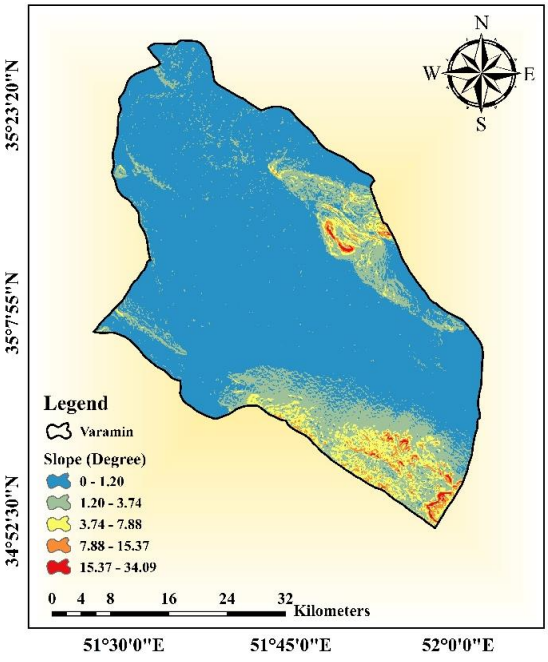
N
W
E
S
35°23'20"N
35°7'55"N
34°52'30"N
Legend
Varamin
Slope (Degree)
0 - 1.20
1.20 - 3.74
3.74 - 7.88
7.88 - 15.37
15.37 - 34.09
0 4 8 16 24 32
Kilometers
51°30'0"E
51°45'0"E
52°0'0"E

(b)

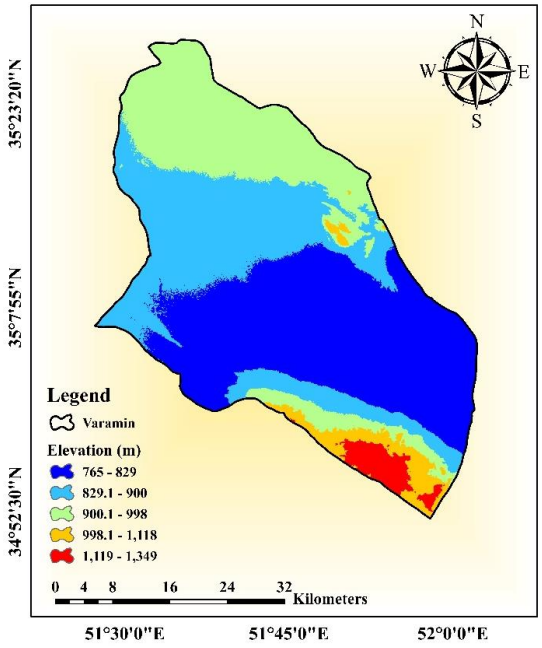
N
W
E
S
35°23'20"N
35°7'55"N
34°52'30"N
Legend
Varamin
Elevation (m)
765 - 829
829.1 - 900
900.1 - 998
998.1 - 1,118
1,119 - 1,349
0 4 8 16 24 32
Kilometers
51°30'0"E
51°45'0"E
52°0'0"E

(c)

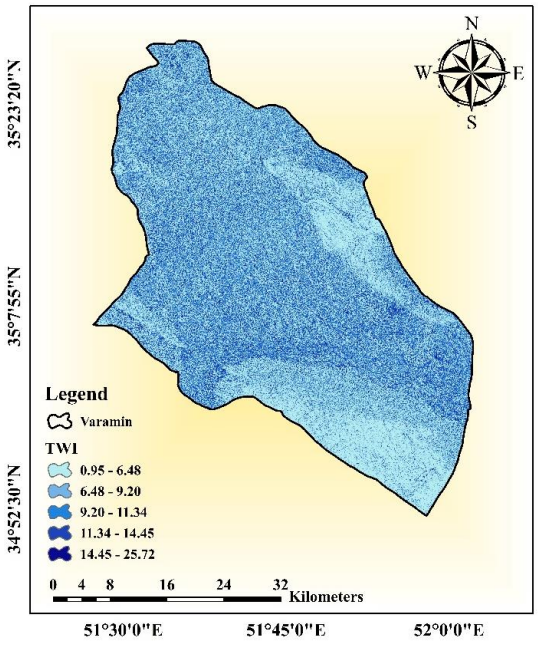
N
W
E
S
35°23'20"N
35°7'55"N
34°52'30"N
Legend
Varamin
TWI
0.95 - 6.48
6.48 - 9.20
9.20 - 11.34
11.34 - 14.45
14.45 - 25.72
0 4 8 16 24 32
Kilometers
51°30'0"E
51°45'0"E
52°0'0"E

(d)

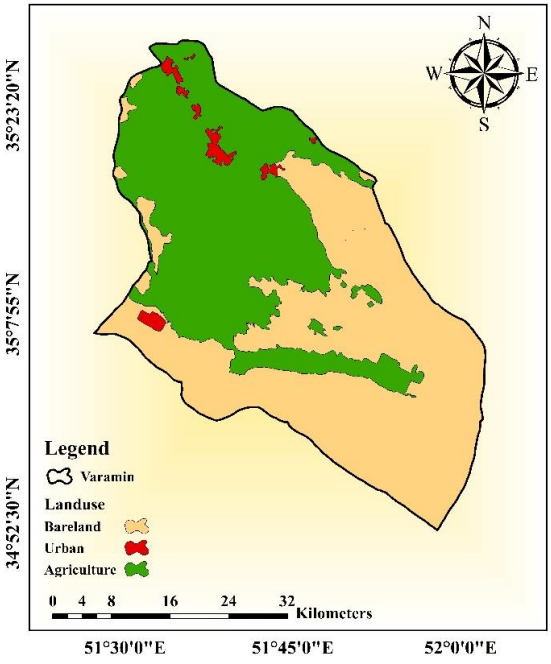
N
W
E
S
35°23'20"N
35°7'55"N
34°52'30"N
Legend
Varamin
Landuse
Bareland
Urban
Agriculture
0 4 8 16 24 32
Kilometers
51°30'0"E
51°45'0"E
52°0'0"E

(e)

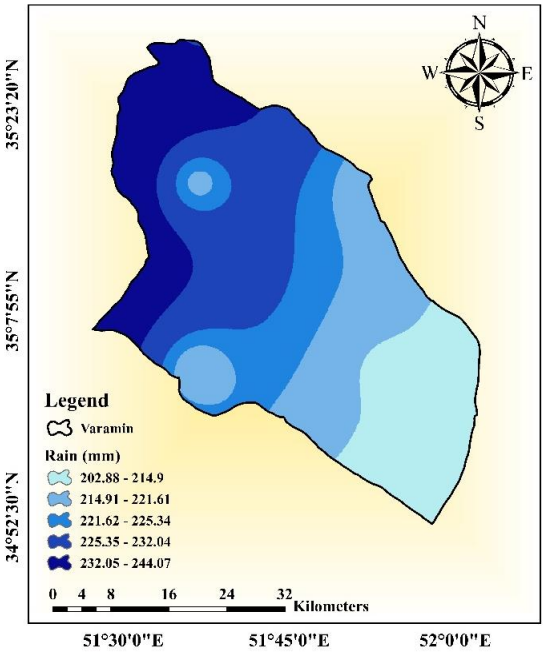
N
W
E
S
35°23'20"N
35°7'55"N
34°52'30"N
Legend
Varamin
Rain (mm)
202.88 - 214.9
214.91 - 221.61
221.62 - 225.34
225.35 - 232.04
232.05 - 244.07
0 4 8 16 24 32
Kilometers
51°30'0"E
51°45'0"E
52°0'0"E

(f)

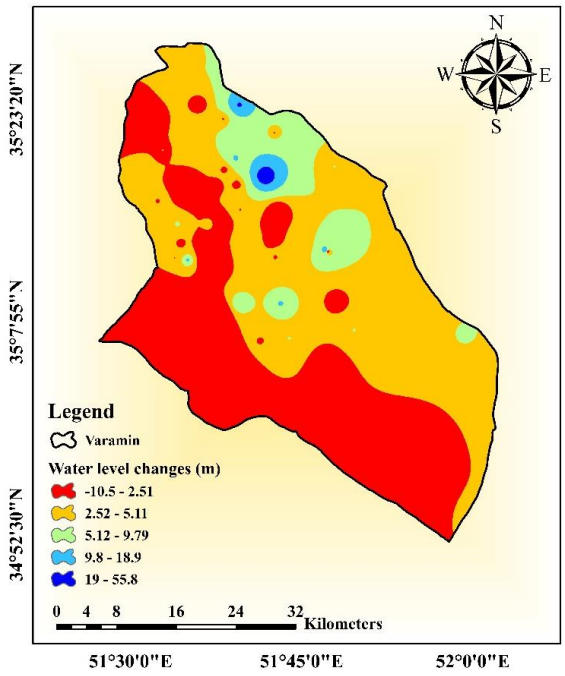

(g)

Figure. 2 - The layers used include (a) soil type, (b) slope, (c) elevation, (d) TWI, (e) land use, (f) rain, and (g) groundwater level

The images used in this research were Sentinel-1 satellite images. Sentinel-1 is a space mission funded by the European Union and implemented by the European Space Agency in the form of the Copernicus program. It consists of two satellites, Sentinel 1-A and Sentinel 1-B, which have the same orbit. Its rotation orbit is that of the Sun, which passes near the polar point at about 98.18 degrees. It rotates around the globe every 12 days and covers the entire surface of the earth every 175 revolutions worldwide.

This satellite captures images in microwave wavelength and C band range, providing data in all weather conditions, day and night. This sensor has a spatial resolution of fewer than 5 meters and a sampling width of up to 400 km. The general specifications of the satellite can be seen in Table 1.

Table 1- General characteristics of Sentinel-1 satellite

Sattelite	Launch Date	Orbit Type	Orbital altitude(km)	Sensor complement
Sentinel1-A	2014/04/03	SSO (Sun-synchronous Orbit)	693	C-SAR
Sentinel1-B	2016/04/22	12 days repeat the cycle		(C-band Synthetic Aperture Radar)

Sentinel-1 provides data continuity from the ENVISAT and European remote sensing satellite missions with data review, coverage, timeliness, and reliability improvements. A summary of the

uses of this satellite is as follows:
(1) Monitoring the frozen areas of the seas and arctic environment and taking care of marine environments
(2) Monitoring of ground-level hazards
(3) Land, forest, water, and soil mapping
(4) Relief support in times of crisis and natural hazards
The images used in this research can be seen in Table 2, along with the date of their capture and the characteristics of the pictures.

Table 2 - Specifications of remote sensing images and date of data collection

Sattelite	Date	Type of data	Mode	Band	Pass	Polarization
Sentinel1-A	2014/10/19	SLC	IW	C-Band	Ascending	VV
	2015/10/02	SLC	IW	C-Band	Ascending	VV
	2016/10/22	SLC	IW	C-Band	Ascending	VV
	2017/10/15	SLC	IW	C-Band	Ascending	VV/VH
	2018/10/22	SLC	IW	C-Band	Ascending	VV/VH

2.3. Methods

In Figure 3, a general flowchart of the proposed method of this study is presented, and in the following, the methods used are introduced in more detail.

2.3.1. Geometric mean methods

The basis of the geometric mean method is based on the matrix of pairwise comparisons. The matrix of pairwise comparisons is done by valuing the row element compared to the column element, and an interval scale between 1 and 9 is usually used for valuation. The higher the given value is, the more the row element is preferable to the column element. 9 indicates extreme importance , and 1 indicates priority and equal importance. Table 1 shows different values and the amount of priority equivalent to each. The figures between the scores in Table 3 have intermediate values.

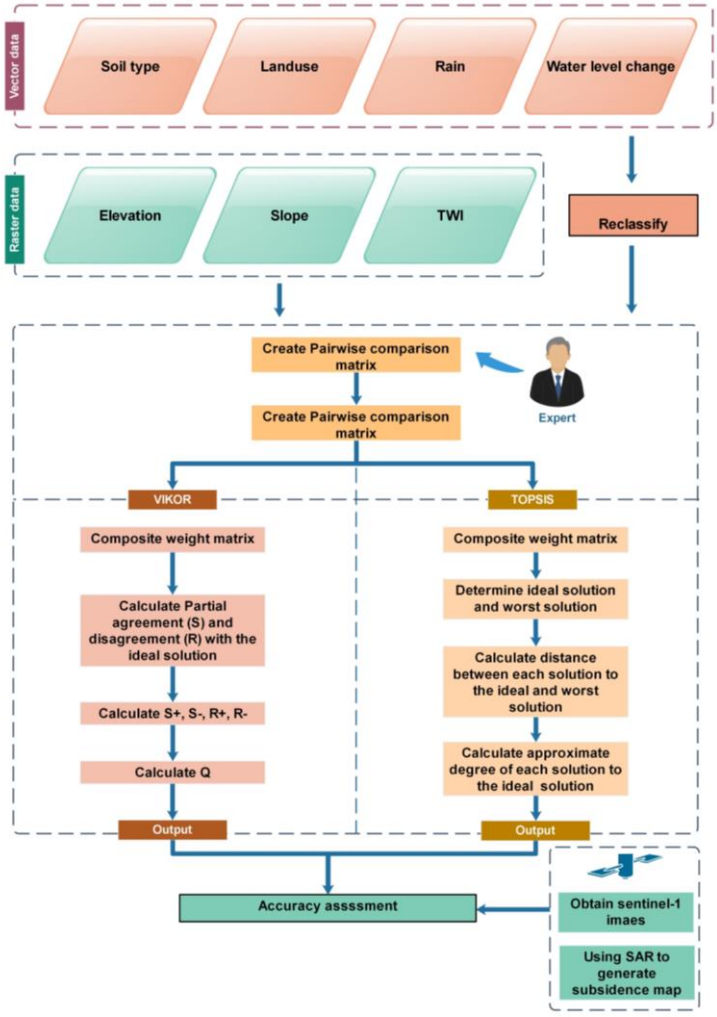

Figure.3 - Flowchart of the proposed method

Table 3- How to value preference in the matrix of paired comparisons

Degree of preference	Scale
Equal importance	1
Equal importance	3
Equal importance	5
Very strong importance	7
Extreme importance	9

The geometric mean method consists of two steps. In the first step, the row values of the matrix of pairwise comparisons are multiplied according to equation 1, and its m-th root is calculated.

$$\mu_i = \sqrt[m]{\prod_{j=1}^{m} a_{ij}} \quad (1)$$

Where m is the number of criteria and the priority value of the i-th criterion over the jth criterion. In the second step, the values obtained in the previous step, according to equation 2, are divided by their sum to reach the weight value of the corresponding criterion.

$$w_i = \frac{\mu_i}{\sum_{i=1}^{m} \mu_i} \quad (2)$$

Which is the weight value of the i-th criterion. The obtained weight values are between zero and one, so the sum of the weight values equals one.

VIKOR

2.3.2. VIKOR

Opricovic presented this method in 1998 [1]. This method ranks the options by calculating how close each option is to the ideal solution, which takes the decision matrix and the vector of weights as input. In the first stage, normalization should be done with equation 3.

$$r_{ij} = \frac{|a_j^+ - a_{ij}|}{|a_j^+ - a_j^-|} \quad (3)$$

that a_j^+ and a_j^- are , respectively the best and worst values for the j-th criterion, and a_{ij} and r_{ij} are the values of the decision matrix before and after the normalization process, respectively. The value of r_{ij} is a number between zero and one, the smaller the value, the more preferable that option is. After normalization, the values of the decision matrix must be multiplied by the weight of each criterion to reach the values of the weighted normalization matrix (t_{ij}). In the next step, partial agreement with the ideal answer (S_i) and partial disagreement with the ideal asolutionR_i) should be calculated according to equations 4 and 5.

$$S_i = \sum_{i=1}^{n} t_{ij} \quad (4)$$

$$R_i = \max_{j \in J} (t_{ij}) \quad (5)$$

This method uses a linear relationship regarding S_i and R_i to evaluate and rank options, defined according to equation 6.

$$Q_i = v \times \left(\frac{S_i - S^+}{S^- - S^+}\right) + (1-v) \times \left(\frac{R_i - R^+}{R^- - R^+}\right) \quad (6)$$

In equation 6, the value v is the weight of the overall desirability, which shows the effect of partial agreement with the ideal answer in the ranking process, and the complement of this value is *1-v.* It gives the degree of influence of partial opposition to the ideal solution. , so S^+ ،S^-،R^+ *and* R^- are obtained according to the equation 7.

$$\begin{cases} S^{+} = \min(S_i) \\ S^{-} = \max(S_i) \end{cases}, \begin{cases} R^{+} = \min(R_i) \\ R^{-} = \max(R_i) \end{cases} \quad (7)$$

2.3.3. TOPSIS

The TOPSIS technique presented in [2] is one of the most practical methods in the field of MCDM. The performance basis of this technique is based on the distance between the ideal positive and negative solution. In this way, the closer an option is to the ideal positive solution, and the further it is from the ideal negative solution, the more suitable it is. The positive ideal solution is hypothetical with the best value of all options. In the same way, the ideal negative solution is the answer that has the worst values of all options. The necessary information for using this technique is the decision matrix and the weight of the criteria. In this study, the criteria's weight was obtained using the geometric mean method. To implement this technique, first, the decision matrix should be normalized according to the Euclidean method according to equation 8.

$$r_{ij} = \frac{a_{ij}}{\sqrt{\sum_{j=1}^{J} a_{ij}^2}} \quad (8)$$

That r_{ij} normalized value, a_{ij} is the value of the i-th option in the j-th criterion, and J is the number of criteria. In the next step, the weighted dimensionless value, according to equation 9, is obtained by multiplying the weight of each criterion by the normalized values.

$$t_{ij} = r_{ij} \times w_j \quad (9)$$

Which w_j is the weight corresponding to the j-th criterion. After that, the ideal positive and negative answers should be determined. The ideal positive answer is the largest value for criteria that are positive in nature, and the smallest value for criteria that are negative in nature. Likewise, the ideal negative answer is defined as the largest value for negative criteria and the smallest value for positive criteria. After the positive and negative ideal answers have been determined, the distance between the options from these two answers should be calculated according to equations 10 and 11, which are indicated by d^{+} and d^{-} respectively.

$$d^{+} = \sqrt{\sum_{j=1}^{J} (t_{ij} - s_j^{+})^2} \quad (10)$$

$$d^{-} = \sqrt{\sum_{j=1}^{J} (t_{ij} - s_j^{-})^2} \quad (11)$$

That s_j^{+} and s_j^{-} are respectively positive and negative values of the ideal answer in the jth criterion. After that, the value of relative proximity should be calculated for all the options, which is done using equation 12.

$$C_i = \frac{d^-}{d^+ + d^-} \quad (12)$$

Which C_i is the degree of relative closeness to the ideal solution for the i-th option. This numerical index is between zero and one, and the larger its value, the closer the option is to the ideal solution. Therefore, the options should be sorted in descending order based on the value to rank the options based on this index.

2.3.4. Differential Interferometric Synthetic Aperture Radar (DInSAR)

In this research, by using Differential Interferometric Synthetic Aperture Radar (DInSAR) method, subsidence was calculated in the Varamin plain area. The interferogram is obtained from the product of one image in the complex conjugate of the second image. Therefore, the amplitude of the interferometer is equal to the product of the amplitude of the two primary images and the phase of the interferometer, the phase difference between these two images. The phase difference between two images is affected by various factors, so it is necessary to remove the effect of disturbing factors to use it. Equation 13 shows the influential factors in the interferometric phase [3].

$$\phi_{\text{int}} = W(\phi_{topo} + \phi_{def} + \phi_{FE} + \phi_{noise} + \phi_{atm} + \phi_{orb}) \quad (13)$$

where ϕ_{int} is the phase of the interferometer, ϕ_{topo} is the topography phase, ϕ_{def} is the phase due to changes in height, ϕ_{FE} is the phase due to the change in the viewing angle of the sensor along the azimuth or flat ground, ϕ_{noise} is the phase caused by noise, ϕ_{atm} is the phase related to the atmosphere, and ϕ_{orb} the phase is caused by It is caused by the circuit error of the gauge. Since the phase of the interferometer has a value between $-\pi$ and $+\pi$, the function W in equation (13) represents the transformation of the phase to the desired range [4]. Any displacement from the radar view is shown as a phase difference between two images before and after the shape of the earth's surface changes.

Mathematically, the scalar change measured by the radar in the distance between the sensor and the ground is equal to the displacement vector in the direction of the radar axis. In this way, by removing the orbital component, the topography of the region, and the atmosphere, the numerical image of the interferometer can be obtained, whose pixel phase difference is only caused by the displacement of the earth's surface [5]. Then by applying the coordinate system on the obtained image, the subsidence map of the area is obtained.

3. Results

3.1. Weighting criteria

Different layers were prepared first to prepare a zoning map of the risk of subsidence for the Varamin, Pishva, and Qarchak regions. The geometric weighting method was used to weigh the different layers, which required a pairwise comparison matrix. To prepare the matrix of pairwise comparisons, a related expert was consulted, the result of which is shown in Table 4.

Table 4 - matrix of paired comparisons

	Groundwater level	Rainfall	Slope	Elevation	TWI	Land use	Soil type
Groundwater level	1	5	7	7	6	0.33	7
Rainfall	1	1	7	7	5	0.2	5
Slope	0.143	0.143	1	0.33	0.33	0.111	0.33
Elevation	0.143	0.143	3	1	1	0.111	0.5
TWI	0.167	0.3	3	1	1	0.111	0.5
Landuse	3	5	9	9	9	1	8
Soil type	0.143	0.2	3	2	2	0.125	1

According to the approach of calculating the weight of each layer in this study, first, the values of points in each row were multiplied together, and the value of the seventh root of the result was calculated. Considering that the number of layers was seven, the seventh root was the product of the criterion. After calculating the seventh root, the obtained values were normalized so that the obtained value for each row was divided by the sum of the obtained values (seventh roots). The calculation method is shown in Table 5.

Table 5 - Weight of each layer

Layer	Multiplied value	The seventh root	Final value
Groundwater level	3395.7	3.1946	0.2699
Rainfall	49	1.7436	0.1473
Slope	0.00008	0.2606	0.0220
Elevation	0.00340	0.4440	0.0375
TWI	0.00556	0.4763	0.0402
Landuse	87480	5.0814	0.4292
Soil type	0.0429	0.6377	0.0539

3.2. Generation of potential subsidence maps

After calculating the weight of the main layers, the layers were entered into the VIKOR and TOPSIS algorithms to combine and produce subsidence potential maps. These methods are presented based on the compatibility or incompatibility of the desired layers in creating the relevant goal, i.e., the potential of subsidence and the effect of each layer should be determined. The effect of layers in creating the subsidence phenomenon in this study is shown in Table 6.

Table 6 - The state of compatibility of layers with the subsidence phenomenon

Layer	Compatibility	Weight
Groundwater level	Incompatibility	0.2699
Rain	Incompatibility	0.1473
Slope	Incompatibility	0.0220

Elevation	Incompatibility	0.0375
TWI	Compatibility	0.0402

According to Table 6, the layers of the underground water level, rain, slope, and elevation are considered incompatible based on the [6]; that is, the lower the value in these layers, the more effective they are in creating the phenomenon of subsidence. Also, the TWI layer has been considered compatible based on [6], which means that the higher the value in this layer, the greater its effect on the subsidence phenomenon. Also, considering that the two layers of soil type and land use are nominally considered[6], a rank has been considered for each class, and this rank has been determined in such a way that the lower the value, the greater the effect on The phenomenon of subsidence occurs. The ranking of the sub-criteria for these two layers, i.e., soil type and land use, is shown in Table 7.

Table 7 - sub-criteria ranks for two layers of soil type and land use

Layer	Sub-criteria	Rank
Soil type	Entisols/aridsols	1
	Aridsols	2
	Salt flats	3
	Bad lands	4
	Rocky lands	5
Land Use	Agriculture	1
	Urban	2
	Bareland	3

Therefore, according to Table 7, Entisols/aridsols have the most effect, and Rocky lands have the least effect on the subsidence phenomenon. Also, agricultural and bareland land uses, respectively, have the most and the least effect on the occurrence of subsidence phenomenon. For these layers, which were of polygon type, the layers were first converted into a raster format. In the following, TOPSIS and VIKOR implementation process is explained in order.

3.3. Implementation of VIKOR

To implement the VIKOR algorithm, normalization of the information layers based on equation 3 was done at first. After normalization, the layers were multiplied by the obtained weight for that layer (Table 5), and the weighted normal layer was obtained. In the next step, the layers of partial agreement with the ideal solution (S_i) and partial disagreement with the ideal solution (R_i) were calculated. S_i was obtained by summing the normal layers according to equation 4. Also, according to equation 5, R_i was obtained by applying the maximum operator on the layers. These two layers are shown in Figure 4.

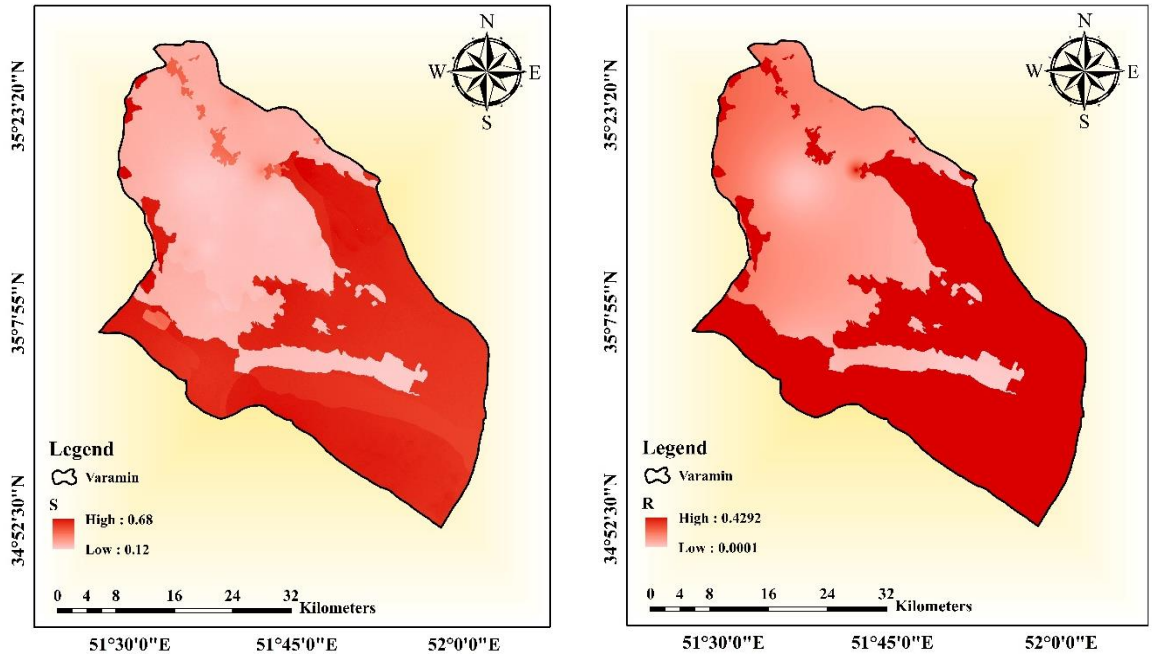

Figure . 4 - S (left) and R (right) layers

After calculating S_i and R_i, the values S^+ ،S^-،R^+ and R^- were calculated according to equation 7 and were placed in equation 6 to obtain the value of Q_i. For this purpose, the overall utility value (v) equals 0.5. Table 8 shows the values S^+ ،S^-،R^+ and R^- shown.

Table 8 – S^+, S-, R^+, R^- Values

S^+=0.116146	R^+=0.0001
S^-=0.683562	R^-=0.4292

3.4. Implementation of TOPSIS

To implement the TOPSIS method, at first, using equations 8 and 9, the weighted normalized values were calculated for each layer. Then the best (positive ideal) and worst (negative ideal) values for each layer were obtained according to the compatibility or incompatibility of the corresponding layer. In this way, the best and worst values were considered for the layers of underground water level, rain, slope, soil type, land use, and elevation. Also, for the TWI layer, the best and worst values were considered the highest and lowest, respectively. In equations 10 and 11, they are shown. In the next step, the distance of each alternative (pixel) to the ideal positive (d^+) and negative (d^-) was calculated according to equations 10 and 11. In Figure 5, layers are shown.

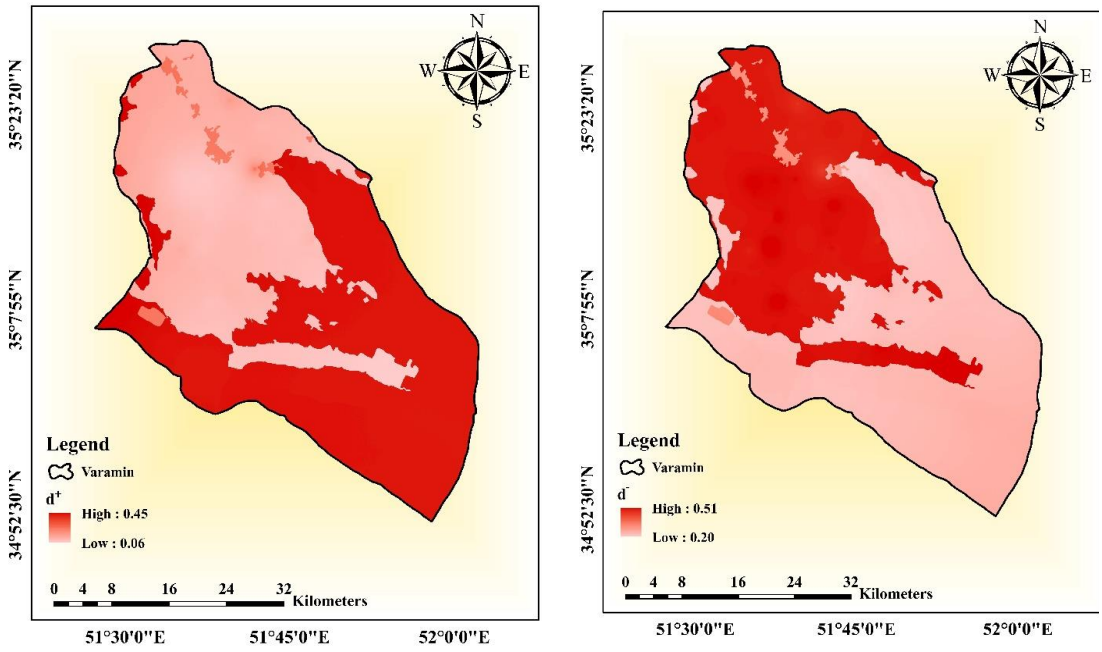

Figure . 5 - d^+ (left) and d^- (right) layers

Therefore, the VIKOR and TOPSIS methods produced two separate subsidence event potential maps, shown in Figure 6 of the output maps of these two methods.

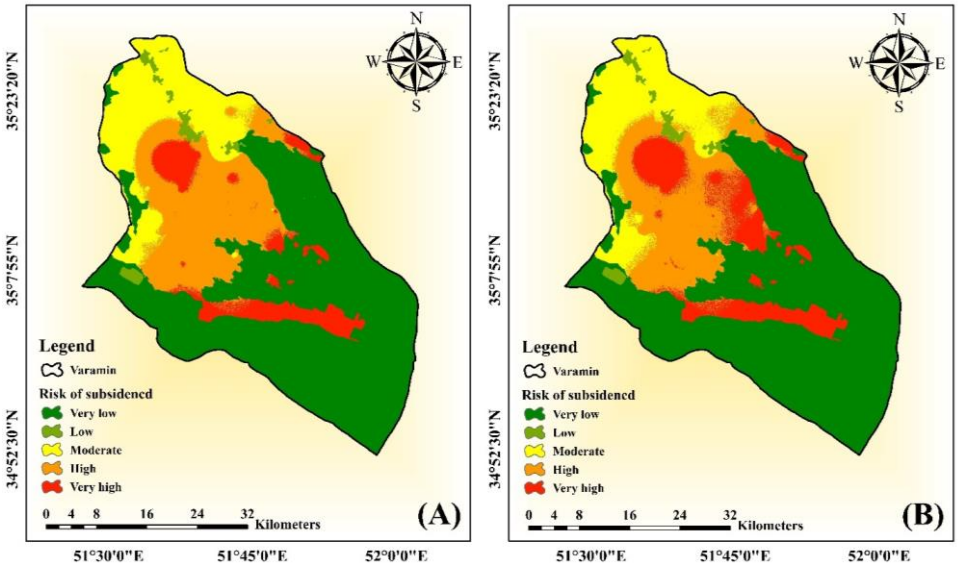

Figure. 6 - Subsidence risk maps resulting from (A)VIKOR and (B)TOPSIS methods

As shown in Figure 6, Varamin, Qarchak, and Pishva regions do not have the same conditions for the entire region regarding the risk of subsidence. In the central and northern areas, more risk is discovered. Based on the results obtained from the VIKOR method, 22247 hectares of the region were classified under very high risk conditions, 34020 hectares under high risk conditions, 29348

hectares under moderate risk conditions, 2847 hectares under low risk conditions, and 101466 hectares under very low risk conditions. Also, based on the results obtained from the TOPSIS method, 15065 hectares of the region were classified under very high risk conditions, 39425 hectares under high risk conditions, 31157 hectares under moderate risk conditions, 2818 hectares under low risk conditions, and 101463 hectares under very low risk conditions. Therefore, it can be said that VIKOR and TOPSIS methods have performed almost similarly in detecting very low risk, low risk, and moderate risk areas, but some differences have been seen in, high risk, and very high risk areas, as shown in Table 9.

Table 9- Area (in hectares) and percentage of different classes based on TOPSIS and VIKOR methods

Class	TOPSIS	VIKOR	| VIKOR-TOPSIS |
Very low	101463 (53.42%)	101466 (53.42%)	3 (0.00%)
Low	2818 (1.48%)	2847 (1.50%)	29 (0.02%)
Moderate	31157 (16.41%)	29348 (15.45%)	1809 (0.95%)
High	39425 (20.76%)	34020 (17.92%)	5405 (2.86%)
Very high	15065 (7.93%)	22247 (11.71%)	7182 (3.78%)

3.5. Subsidence map using radar interferometry

In this section, the land surface subsidence was calculated using Sentinel-1 images. First, the phase of each image was calculated based on equation 13, and then the displacement of the earth's surface was obtained from the phase difference between the two images. Figure 7 shows the map related to displacement.

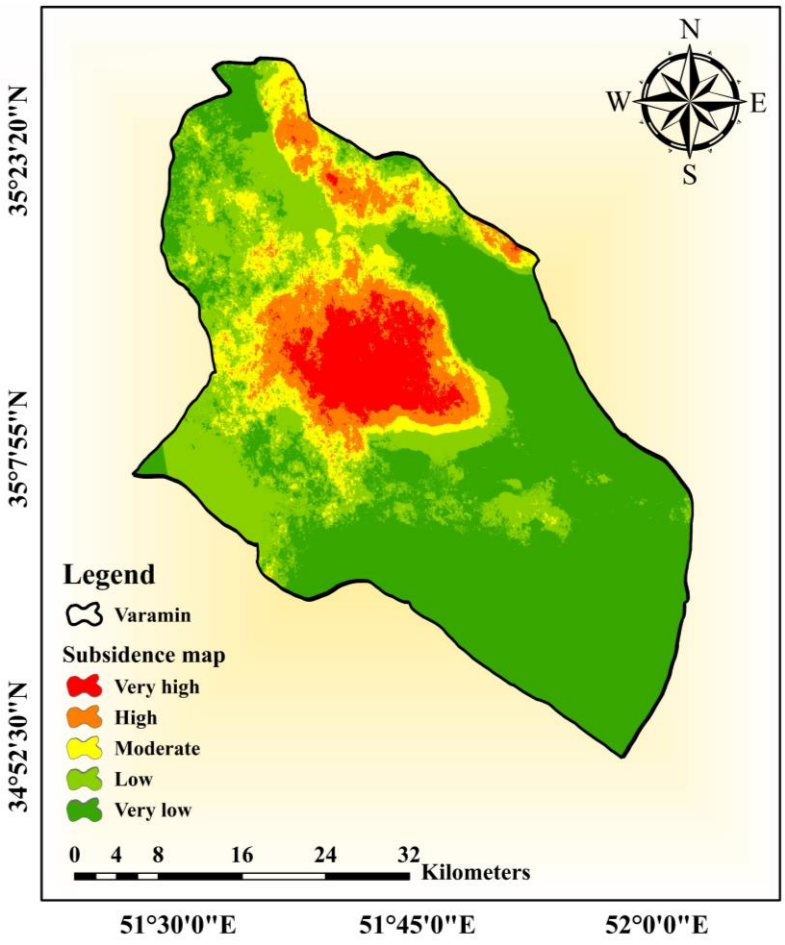

Figure. 7 - Subsidence map for the years 2014 to 2018 using the DInSAR technique

4. Discussion

To evaluate the reliability of the maps obtained from TOPSIS and VIKOR methods, the subsidence map based on the years 2014 to 2018 was considered reference data, and based on the comparison, appropriate adaptability was obtained. The evaluation method was that the subsidence risk maps were classified using different methods. The subsidence occurrence map based on DInSAR was also classified with the same classification method, then the degree of similarity of the pixels was evaluated by overlapping the classified layers. The classification methods used in this study include quintile, natural break, geometric interval, and equal interval. Table 10 shows the percentage of similarity and dissimilarity of potential map and subsidence occurrences according to different classification methods, shown separately for each method.

Table 10- Evaluating the degree of similarity between the potential map and the event map according to different classification methods

Classification methods	Similarity/Dissimilarity	TOPSIS	VIKOR
Quantile	Similarity	73.50	78.86
	Dissimilarity	26.50	21.14
Geometric Interval	Similarity	80.82	78.64

	Dissimilarity	19.18	21.36
Natural break	Similarity	82.24	81.80
	Dissimilarity	17.76	18.20
Equal Interval	Similarity	62.11	62.23
	Dissimilarity	37.89	37.77

As shown in Table 10, how maps are classified significantly affects the similarity of the reference map with the produced maps. For example, when the natural break and geometric interval methods are chosen, the similarity rate has reached above 80%, while the similarity rate for the quantile method is between 70 and 80%. For the equal interval method, it is in the range of 62%. Combining the layers has also been effective in the amount of similarity. In some cases, the VIKOR method has been better; in others, the TOPSIS method has worked better. For example, when the natural break and geometric methods are selected, the potential map obtained by the TOPSIS method compared to the VIKOR method has a higher degree of similarity with the occurrence map, so that for the geometric interval mode, the similarity is 80.82 and 78.64% for TOPSIS and VIKOR methods, respectively. Also, for the natural break mode, the degree of similarity was 82.24 and 81.80%, respectively, for TOPSIS and VIKOR methods. Also, when the quantile and equal interval methods were selected, the potential map resulting from the VIKOR method had more similarity with the occurrence map compared With the TOPSIS method, so for the quantile method, the similarity was 78.86% and 73.50% for the VIKOR and TOPSIS methods, respectively. Also, the similarity rate for the equal interval mode was 62.23 and 62.11% for VIKOR and TOPSIS methods, respectively.

5. Conclusion

The results obtained from the TOPSIS and VIKOR methods indicate that approximately 28.69% and 29.63% of the studied area, respectively, are at high risk of subsidence. Upon examining satellite images of these high-risk areas, it's apparent that they are predominantly used for agricultural purposes. The high water consumption associated with agriculture, along with the subsequent depletion of underground aquifers, plays a significant role in the occurrence of subsidence in these regions. Conversely, based on the TOPSIS and VIKOR methods, approximately 54.90% and 54.92% of the area, respectively, exhibit a low risk of subsidence, with most of these areas located in the southern parts of the region. These southern regions are primarily characterized by bareland and salt marsh soil types. In these areas, the underground water level is relatively favorable, contributing to a lower risk of subsidence.

Intermediate risk areas cover about 16.41% of the total area according to the TOPSIS method, and approximately 15.45% of the total area, according to the VIKOR method, is situated in the western parts of the region. These areas are also characterized by bareland, but their underground water conditions are not as favorable. If other subsidence-inducing factors come into play in these areas, they too could witness subsidence phenomena. Comparing the maps produced by the TOPSIS and VIKOR methods with the radar interferometric method, it is evident that these two approaches can reasonably determine the occurrence of subsidence. The integration of GIS tools and various layers enables the creation of maps that closely resemble reality, aiding decision-makers and city managers in developing suitable policies to address the subsidence crisis. One notable advantage of GIS and MCDM methods is their ability to generate periodic maps for the region based on different factors, which can be done more quickly compared to radar image processing techniques, which are more time-consuming.

It's worth noting that the weights assigned to layers in the study were based on expert opinions, which may introduce a degree of uncertainty. Future studies could benefit from efforts to reduce this uncertainty. Additionally, the use of artificial intelligence methods and remote sensing

techniques can further enhance the accuracy of evaluating the factors contributing to subsidence and zoning risk areas.

Declarations

Funding Information (Not fund)

Conflict of Interest /Competing interests (None)

Availability of Data and Material (Data are not available)

Consent to Publish (Authors consent to publishing)

Authors Contributions (All co-authors contributed to the manuscript)

Code availability (Not available)

REFERENCES

Abdollahi, S., Pourghasemi, H. R., Ghanbarian, G. A., & Safaeian, R. (2019). Prioritization of effective factors in the occurrence of land subsidence and its susceptibility mapping using an SVM model and their different kernel functions. *Bulletin of Engineering Geology and the Environment*, *78*(6), 4017-4034. https://doi.org/10.1007/s10064-018-1403-6

Abedini, M., Aghayary, l., & Asghari Saraskanrood, S. (2023). Evaluating and Zoning Subsidence Risk using MABAC and ANP Adaptive Algorithm (Case Study: Ardabil Plain). *Journal of Geography and Environmental Hazards*, *11*(4), 43-68. https://doi.org/10.22067/geoeh.2022.74202.1143

Anderssohn, J., Wetzel, H.-U., Walter, T. R., Motagh, M., Djamour, Y., & Kaufmann, H. (2008). Land subsidence pattern controlled by old alpine basement faults in the Kashmar Valley, northeast Iran: results from InSAR and levelling. *Geophysical Journal International*, *174*(1), 287-294. https://doi.org/10.1111/j.1365-246X.2008.03805.x

Arabameri, A., Pal, S. C., Rezaie, F., Chakrabortty, R., Chowdhuri, I., Blaschke, T., & Ngo, P. T. T. (2021). Comparison of multi-criteria and artificial intelligence models for land-subsidence susceptibility zonation. *Journal of Environmental Management*, *284*, 112067. https://doi.org/10.1016/j.jenvman.2021.112067

Calderhead, A. I., Therrien, R., Rivera, A., Martel, R., & Garfias, J. (2011). Simulating pumping-induced regional land subsidence with the use of InSAR and field data in the Toluca Valley, Mexico. *Advances in Water Resources*, *34*(1), 83-97. https://doi.org/10.1016/j.advwatres.2010.09.017

Dehghani, M., Zoej, M. J. V., Hooper, A., Hanssen, R. F., Entezam, I., & Saatchi, S. (2013). Hybrid conventional and persistent scatterer SAR interferometry for land subsidence monitoring in the Tehran Basin, Iran. *ISPRS journal of photogrammetry and remote sensing*, *79*, 157-170. https://doi.org/10.1016/j.isprsjprs.2013.02.012

Ebrahimy, H., Feizizadeh, B., Salmani, S., & Azadi, H. (2020). A comparative study of land subsidence susceptibility mapping of Tasuj plane, Iran, using boosted regression tree, random forest and classification and regression tree methods. *Environmental Earth Sciences*, *79*, 1-12. https://doi.org/10.1007/s12665-020-08953-0

Galloway, D. L., Jones, D. R., & Ingebritsen, S. E. (1999). *Land subsidence in the United States* (Vol. 1182). US Geological Survey.

Galve, J., Gutiérrez, F., Lucha, P., Guerrero, J., Bonachea, J., Remondo, J., & Cendrero, A. (2009). Probabilistic sinkhole modelling for hazard assessment. *Earth Surface Processes and Landforms*, *34*(3), 437-452. https://doi.org/10.1002/esp.1753

Herrera-García, G., Ezquerro, P., Tomás, R., Béjar-Pizarro, M., López-Vinielles, J., Rossi, M., Mateos, R. M., Carreón-Freyre, D., Lambert, J., & Teatini, P. (2021). Mapping the global threat of land subsidence. *Science*, *371*(6524), 34-36. https://doi.org/10.1126/science.abb8549

Hwang, C.-L., Yoon, K., Hwang, C.-L., & Yoon, K. (1981). Methods for multiple attribute decision making. *Multiple attribute decision making: methods and applications a state-of-the-art survey*, 58-191. https://doi.org/10.1007/978-3-642-48318-9-3

Kidanu, S. T., Anderson, N. L., & Rogers, J. D. (2018). Using GIS-based spatial analysis to determine factors influencing the formation of sinkholes in Greene County, Missouri. *Environmental & Engineering Geoscience*, *24*(3), 251-261. https://doi.org/10.2113/EEG-2014

Lee, S., Park, I., & Choi, J.-K. (2012). Spatial Prediction of Ground Subsidence Susceptibility Using an Artificial Neural Network. *Environmental Management*, *49*(2), 347-358. https://doi.org/10.1007/s00267-011-9766-5

Mehrnoor, S., Robati, M., Kheirkhah Zarkesh, M. M., Farsad, F., & Baikpour, S. (2023). Land Subsidence Hazard Zoning in Hashtgerd Plain based on Integrated Multi-Criteria Decision-Making Approach: WOI-BWM. *Journal of Geography and Environmental Hazards*, *11*(4), 127-148. https://doi.org/10.22067/geoeh.2022.75445.1188

Mohammady, M., Pourghasemi, H. R., & Amiri, M. (2019). Land subsidence susceptibility assessment using random forest machine learning algorithm. *Environmental Earth Sciences*, *78*, 1-12. https://doi.org/10.1007/s12665-019-8518-3

Mohammady, M., Pourghasemi, H. R., Amiri, M., & Tiefenbacher, J. P. (2021). Spatial modeling of susceptibility to subsidence using machine learning techniques. *Stochastic Environmental Research and Risk Assessment*, 1-12. https://doi.org/10.1007/s00477-020-01967-x

Motagh, M., Djamour, Y., Walter, T. R., Wetzel, H.-U., Zschau, J., & Arabi, S. (2007). Land subsidence in Mashhad Valley, northeast Iran: results from InSAR, levelling and GPS. *Geophysical Journal International*, *168*(2), 518-526. https://doi.org/10.1111/j.1365-246X.2006.03246.x

Nadiri, A. A., Moazamnia, M., Sadeghfam, S., & Barzegar, R. (2021). Mapping Risk to Land Subsidence: Developing a Two-Level Modeling Strategy by Combining Multi-Criteria Decision-Making and Artificial Intelligence Techniques. *Water*, *13*(19), 2622. https://doi.org/10.3390/w13192622

Najafi, Z., Pourghasemi, H. R., Ghanbarian, G., & Fallah Shamsi, S. R. (2020). Land-subsidence susceptibility zonation using remote sensing, GIS, and probability models in a Google Earth Engine platform. *Environmental Earth Sciences*, *79*, 1-16. https://doi.org/10.1007/s12665-020-09238-2

Opricovic, S. (1998). Multicriteria optimization of civil engineering systems. *Faculty of civil engineering, Belgrade*, *2*(1), 5-21.

Pacheco, J., Arzate, J., Rojas, E., Arroyo, M., Yutsis, V., & Ochoa, G. (2006). Delimitation of ground failure zones due to land subsidence using gravity data and finite element modeling in the Querétaro valley, México. *Engineering Geology*, *84*(3-4), 143-160. https://doi.org/10.1016/j.enggeo.2005.12.003

Tien Bui, D., Shahabi, H., Shirzadi, A., Chapi, K., Pradhan, B., Chen, W., Khosravi, K., Panahi, M., Bin Ahmad, B., & Saro, L. (2018). Land subsidence susceptibility mapping in south korea using machine learning algorithms. *Sensors*, *18*(8), 2464. https://doi.org/10.3390/s18082464

Tomás, R., Romero, R., Mulas, J., Marturià, J. J., Mallorquí, J. J., López-Sánchez, J. M., Herrera, G., Gutiérrez, F., González, P. J., & Fernández, J. (2014). Radar interferometry techniques for the study of ground subsidence phenomena: a review of practical issues through cases in Spain. *Environmental Earth Sciences*, *71*, 163-181. https://doi.org/10.1007/s12665-013-2422-z

Toomanian, A., Kakroodi, A., & Etemadi, M. A. Spatial Modeling of Land Subsidence Using GIS-Based Machine Learning Algorithms. *Available at SSRN 4024231*. https://dx.doi.org/10.2139/ssrn.4024231

Water, M. G. (2000). Land Subsidence in the United States.

© 2023 by the authors. Licensee IAU, Meybod, Iran. This article is an open access article distributed under the terms and conditions of the Creative Commons Attribution (CC BY) license (http://creativecommons.org/licenses/by/4.0/).